Critical Influence of Organic A′-Site Ligand Structure on 2D Perovskite Crystallization

Document license:
TAVERNE

DOI:
[10.1002/smll.202206787](https://doi.org/10.1002/smll.202206787)

Document status and date:
Published: 22/03/2023

Document Version:
Publisher's PDF, also known as Version of Record (includes final page, issue and volume numbers)

Please check the document version of this publication:

• A submitted manuscript is the version of the article upon submission and before peer-review. There can be important differences between the submitted version and the official published version of record. People interested in the research are advised to contact the author for the final version of the publication, or visit the DOI to the publisher's website.
• The final author version and the galley proof are versions of the publication after peer review.
• The final published version features the final layout of the paper including the volume, issue and page numbers.

[Link to publication](#)

Spray Coating Experiments: Setups and Methodologies

13

Thin Films III

Spray Coating Experiments: Setups and Methodologies

EVIDENT OLYMPUS

WILEY

The latest eBook from Advanced Optical Metrology. Download for free.

Spray Coating Experiments: Setups and Methodologies, is the third in our Thin Films eBook series. This publication provides an introduction to spray coating, three article digests from Wiley Online Library and the latest news about Evident's Image of the Year Award 2022.

Wiley in collaboration with Evident, are committed to bridging the gap between fundamental research and industrial applications in the field of optical metrology. We strive to do this by collecting and organizing existing information, making it more accessible and useful for researchers and practitioners alike.

EVIDENT OLYMPUS

WILEY

Critical Influence of Organic A′-Site Ligand Structure on 2D Perovskite Crystallization

Zhaotong Qin, Haibo Xue, Minchao Qin,* Yuhao Li, Xiao Wu, Wei-Ru Wu, Chun-Jen Su, Geert Brocks, Shuxia Tao,* and Xinhui Lu*

Organic A′-site ligand structure plays a crucial role in the crystal growth of 2D perovskites, but the underlying mechanism has not been adequately understood. This problem is tackled by studying the influence of two isomeric A′-site ligands, linear-shaped *n*-butylammonium (*n*-BA$^+$) and branched *iso*-butylammonium (*iso*-BA$^+$), on 2D perovskites from precursor to device, with a combination of in situ grazing-incidence wide-angle X-ray scattering and density functional theory. It is found that branched *iso*-BA$^+$, due to the lower aggregation enthalpies, tends to form large-size clusters in the precursor solution, which can act as pre-nucleation sites to expedite the crystallization of vertically oriented 2D perovskites. Furthermore, *iso*-BA$^+$ is less likely to be incorporated into the MAPbI$_3$ lattice than *n*-BA$^+$, suppressing the formation of unwanted multi-oriented perovskites. These findings well explain the better device performance of 2D perovskite solar cells based on *iso*-BA$^+$ and elucidate the fundamental mechanism of ligand structural impact on 2D perovskite crystallization.

Z. Qin, M. Qin, Y. Li, X. Wu, X. Lu
Department of Physics
The Chinese University of Hong Kong
Shatin, Hong Kong SAR 999077, P. R. China
E-mail: qinminchao@link.cuhk.edu.hk; xinhui.lu@cuhk.edu.hk

H. Xue, G. Brocks, S. Tao
Materials Simulation and Modelling
Department of Applied Physics
Eindhoven University of Technology
P.O. Box 513, Eindhoven 5600 MB, The Netherlands
E-mail: s.x.tao@tue.nl

H. Xue, G. Brocks, S. Tao
Center for Computational Energy Research
Department of Applied Physics
Eindhoven University of Technology
P.O. Box 513, Eindhoven 5600 MB, The Netherlands

W.-R. Wu, C.-J. Su
National Synchrotron Radiation Research Center
Hsinchu Science Park, Hsinchu, Taiwan 30076, R. O. China

G. Brocks
Computational Materials Science
Faculty of Science and Technology and MESA+ Institute for Nanotechnology
University of Twente
P.O. Box 217, Enschede 7500AE, The Netherlands

1. Introduction

2D lead halide perovskite solar cells (PSCs) reduce the dimensionality of 3D perovskites to quasi-2D layered perovskites (abbreviated as "2D perovskite") by the insertion of large organic cations. 2D perovskites can be classified into different types on the basis of the organic spacer used. For instance, perovskites using monovalent ligands are called Ruddlesden–Popper (RP) perovskites,[1] while those using divalent ligands are called Dion–Jacobson (DJ) perovskites;[2] another type is named as ACI perovskite because it employs alternating large and small cations as the interlayer spacer.[3] Particularly, the monovalent organic ligands, for example, butylammonium (BA$^+$)[4–10] and phenylethyl ammonium (PEA$^+$)[11–14] in 2D RP perovskite (with a general formula of A′$_2$A$_{n-1}$Pb$_n$X$_{3n+1}$) are often hydrophobic, thus offering enhanced humidity stability, as well as the tunability in bandgap through quantum confinement.[15–18] However, the device power conversion efficiency (PCE) is sacrificed, especially the short-circuit current density (J_{sc}). In 2016, Tsai et al. first reported a hot-casting method that can arrange 2D perovskite in a vertical direction, significantly improving the PCE compared with the randomly oriented control group.[1] The lower J_{sc} has been found to be attributed to the incorporation of insulating and photo-inactive A′-site ligands, which impede the charge transport within the active layer.[11,15,19,20] To solve this problem, extensive research efforts have been devoted to controlling the growth of vertically oriented 2D perovskite layers, mainly by employing versatile fabrication processes[21,22] and organic ligands.[23,24] In recent years, some heteroatomic and aromatic ligands, such as 2-thiophenemethyl ammonium[25,26] and 4-fluorinated phenylethyl ammonium,[27,28] have also been applied in high-efficiency 2D PSCs.

However, the fundamental mechanism of 2D perovskite crystallization is not fully understood yet. The organic A′ site ligand structure has been found to play a critical role in manipulating the crystal growth of 2D perovskites. For instance, the alkyl chain length of the ligands can affect the formation of the 2D layered crystal structure and phase purity, and hence the optoelectronic properties of the film.[29] The parity of the number of carbon atoms in linear ligands was also reported to influence the orientation of 2D perovskites.[30] Ligands with

isomeric carbon chain structures sharing the same chemical formula have also been found to have significant differences in film properties,[31] but the mechanism remained unknown. Aromatic ligands show extra properties compared to aliphatic ones and tend to be disordered in the crystal structures due to the rigid and planar π-electron-conjugated ring structure, and ligands with heteroatoms, such as halogen, oxygen, and sulfur, involve complicated intra- and inter-molecular hydrogen bonding and electronegativity-induced repulsion, exerting significant influence on the crystal structure of 2D perovskites.[32] For example, fluorinated phenylethyl ammonium ligands that differ in substituent positions of fluorine lead to a different packing geometry between neighboring ligand layers in 2D perovskite films, dictated by the interactions among the highly electronegative fluorine atoms and between the conjugated phenyl ring.[23] The ligand piperazine dihydroiodide used in the formamidinium tin iodide ($FASnI_3$) precursor, is able to induce a 100 nm-level aggregation and pre-nucleation of the $FASnI_3$ perovskite.[33] The roles of these ligands have mainly been correlated with device performance, while the effects of different ligand structures on the crystallization process and the resulting orientations in 2D perovskites have not been investigated. Therefore, a systematic exploration of this aspect is highly desirable to understand and control the crystal growth of 2D perovskites.

State-of-the-art in situ grazing-incidence wide-angle X-ray scattering (GIWAXS) is a powerful tool to monitor the perovskite crystallization pathways by mimicking real fabrication conditions.[34] It has been widely applied to study the effect of different fabrication techniques on growing 2D perovskites. For instance, Hoffman et al. monitored the crystallization process during a room-temperature spin coating procedure, which revealed a general three-stage formation mechanism of 2D perovskites, involving solvates, oriented 3D phases, and 2D phases.[35] Compared to room-temperature spin coating, a hot-casting method can suppress the formation of the solvate phase, according to in situ GIWAXS results, leading to a better-oriented growth of 2D perovskites.[36] Other fabrication techniques, such as anti-solvent treatments and incorporation of additives, have also been reported to alter the 2D perovskite crystallization process, with effect on intermediate phases,[37] crystal orientation,[38] and 2D perovskite distributions in the films with different n values.[39] Besides, the initial crystal growing of 2D perovskites has been found to be the air-liquid interface rather than the substrate.[19]

Herein, we employ in situ GIWAXS to monitor the phase evolution during the film-formation process for 2D perovskites based on two commonly used isomeric A′ site ligands, that is, n-butylammonium (n-BA⁺) and iso-butylammonium (iso-BA⁺). The impact of the ligand structure on the formation of films is comprehensively investigated in terms of crystallization kinetics, precursor solutions, and crystal phase compositions. The underlying mechanism is further analyzed by density functional theory (DFT) calculations. We identify the evolution of vertical 2D and 3D phases independently by focusing on a unique representative peak for each phase. It is demonstrated that, compared to the linear-shaped n-BA⁺, the incorporation of branch-shaped iso-BA⁺ can accelerate the crystallization of 2D perovskites and concurrently inhibits the

formation of unwanted multi-oriented perovskite phases that are observed in n-BA⁺-based counterparts. Consequently, the iso-BA⁺-based films present a higher order of vertical orientation and enhanced film crystallinity. The underlying mechanism is further characterized by dynamic light scattering (DLS) and nuclear magnetic resonance (NMR) measurements. The data suggest that in the iso-BA⁺-contained precursor solution, large clusters are spontaneously formed. This is consistent with the lower enthalpies of accumulation of iso-BA⁺ versus n-BA⁺ ligand, as predicted by DFT calculations. We suggest that these clusters could act as pre-nucleation sites to accelerate the crystallization of 2D perovskites. Furthermore, the linear-shaped n-BA⁺ molecule can be more easily incorporated into a $MAPbI_3$ lattice than the branched iso-BA⁺ molecule, obstructing the long-range stacking of vertically oriented [PbI_6] octahedral frameworks. This work provides a fundamental understanding of the crystallization kinetics of 2D perovskites. It reveals the significant structural impact of organic A′-site ligands on 2D perovskites from precursor to thin films to devices, pointing the way to future optimization of 2D perovskite PSCs based on various ligand structures.

2. Results and Discussion

2.1. Distinct Film Crystalline Structures and Device Performance with Isomeric Ligands

The chemical structures of the two organic ligands, n-BA⁺ and iso-BA⁺, are shown in **Figure 1**a. The former has a linear alkyl chain, while the latter has branched chains. The 2D perovskite films ($A'_2MA_{n-1}Pb_nI_{3n+1}$, <n> = 5) based on the two ligands were prepared by the conventional hot-casting method.[1] It is noted that the n value represents the number of [PbI_6] octahedra layers sandwiched by ligand layers, whereas the <n> value is defined by the stoichiometric ratio in the precursor. The final film should contain 2D perovskites with mixed n values.[37]

The crystalline structure in the 2D perovskite films based on n-BA⁺ and iso-BA⁺ ligands was investigated by ex situ GIWAXS measurements. The measured 2D GIWAXS patterns are presented in Figure 1b,c. The sector intensity profiles versus |q| are plotted in Figure S1a, Supporting Information, to understand the phase composition and overall crystallinity. The peak positions are largely overlapped for both films, indicating similar phase compositions of both films. Obviously, the iso-BA⁺-based film has much higher crystallinity, given the notably larger (101) peak (|q| = 1 Å⁻¹) area (Figure S1a, Supporting Information). The coherence length based on the Scherrer equation[40] for the films based on n-BA⁺ and iso-BA⁺ is 192 (Δq = 0.0295 Å⁻¹) and 277 nm (Δq = 0.0204 Å⁻¹), respectively, indicative of relatively larger crystal domain sizes in the iso-BA⁺-based film. The branched iso-BA⁺-based film exhibits typical clear and discrete scattering peaks, suggesting highly oriented crystalline phases. All of the scattering peaks in the GIWAXS pattern (Figure 1c) can be indexed with vertically oriented 2D perovskite phase with the (101) plane parallel to the substrate, and highly ordered 3D tetragonal $MAPbI_3$ phase with the (101) or (010) plane parallel to the substrate, as demonstrated in Figure 1d and Figure S2, Supporting Information. We name this kind of highly ordered
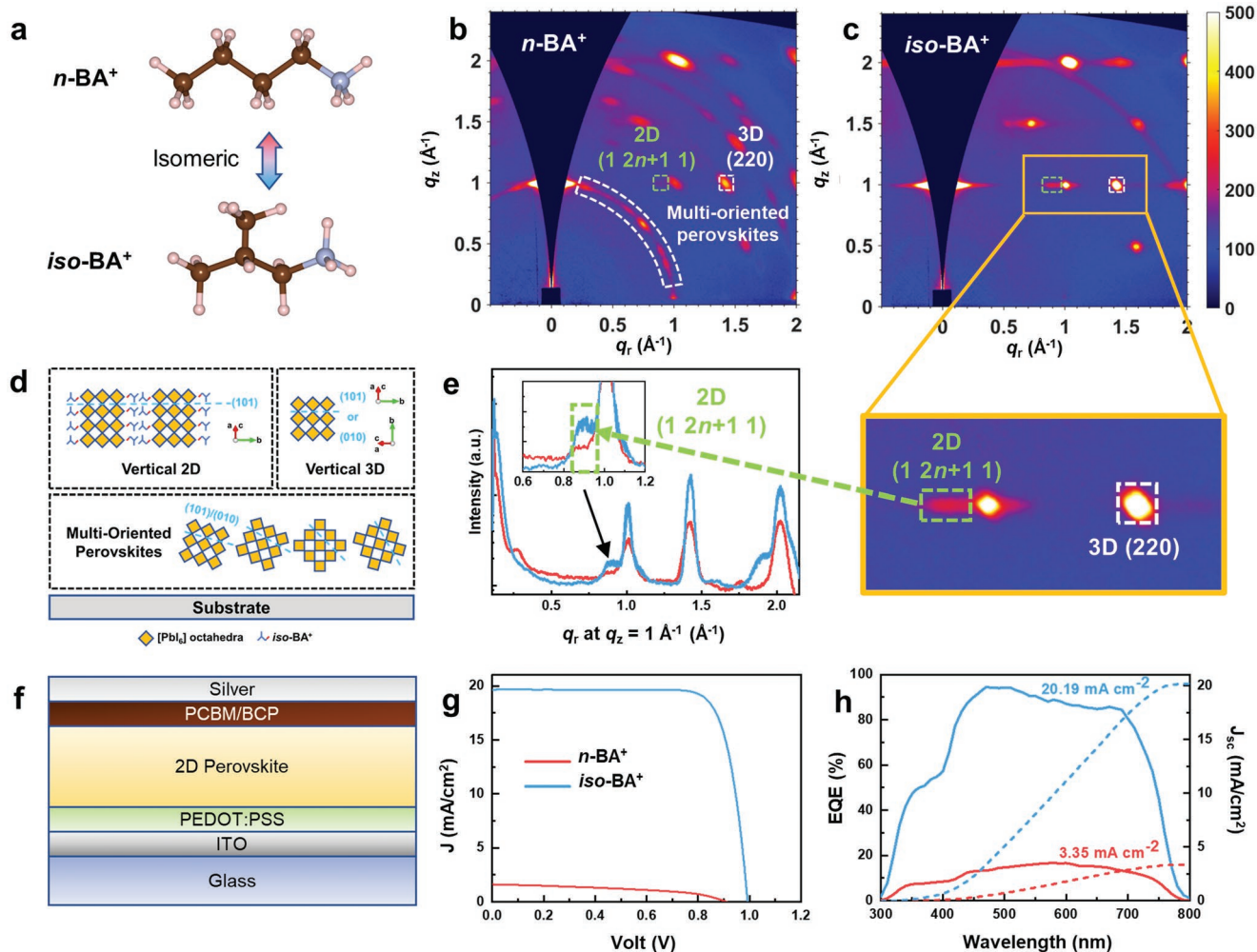
**ADVANCED
SCIENCE NEWS**

www.advancedsciencenews.com

NANO · MICRO

small

www.small-journal.com

Figure 1. Distinct film crystalline structures and device performance with isomeric ligands. a) Chemical structures of *n*-BA+ and *iso*-BA+. b,c) 2D GIWAXS patterns of 2D (<*n*> = 5) perovskite films based on b) *n*-BA+ and c) *iso*-BA+. Representative Bragg peaks of vertical 2D phases, vertical 3D phase, and multi-oriented perovskite phase are marked by blue dashed squares, white dashed squares, and white dashed arc, respectively. d) The schematic diagram of these phases. e) The GIWAXS intensity profiles versus q_r at $q_z = 1$ Å^{-1}. f) The schematic of the inverted perovskite solar cell device structure. g) Current density–voltage (*J–V*) curves of solar cell devices based on the two isomers. See also Figures S15 and S16, Supporting Information, for the full scan results and statistical results. h) The corresponding external quantum efficiency (EQE) spectra and the integral of the current density of typical PSCs based on *n*-BA+ and *iso*-BA+ ligands.

3D perovskite as the "vertical 3D" perovskite phase in this work. The detailed peak indexing for each phase is shown in Figures S3 and S4, Supporting Information. We selected (1 2*n*+1 1) of vertical 2D perovskite phase and (220) of vertical 3D phase as their corresponding representative peaks, due to their uniqueness and no/weak overlapping with other peaks, as highlighted in Figure 1b,c,e. Detailed discussion and explanation about the Bragg peaks for indicating 2D perovskites (e.g., (0 *k* 0) and (1 2*n*+1 1)) can be found in Figures S5 and S6 and Note S1, Supporting Information. The coexistence of 2D and 3D perovskite phases is also confirmed by UV–vis absorption spectra (Figure S7a, Supporting Information), in which both characteristic exciton peaks (~570 nm for *n* = 2, ~610 nm for *n* = 3, and ~645 nm for *n* = 4)[21] of the 2D perovskites and the absorption edge (770 nm) of the 3D perovskites were observed. The bandgaps of the two perovskite films were the same as shown in the Tauc plot in Figure S7b, Supporting Information. In

contrast, the linear *n*-BA+-based film shows supernumerary (101) peaks at different polar angles (χ) (Figure 1b and Figure S1b, Supporting Information), indicating a broad range of crystal orientations, which are denoted as "multi-oriented" perovskite phases in the following as shown in Figure 1d. In short, the alternation from the linear *n*-BA+ ligands to the branched *iso*-BA+ ligands gives rise to the preferential growth of vertical-oriented perovskite crystals and much higher film crystallinity.

To correlate the distinct crystalline structure with the device performance, we fabricated PSCs based on the two films with the inverted device structure of ITO/PEDOT:PSS/perovskite/PC$_{61}$BM/BCP/Ag (Figure 1f), for which the detailed process is presented in the Experimental Section. The *n*-BA+-based devices exhibited very poor performance (Figure 1g and Figures S8 and S9, Supporting Information), mainly due to the extremely low J_{sc}. It is noted that in order to focus on the influence of A′-site ligands, we did not adopt additional treatments during the

deposition of 2D perovskite films such as the incorporation of additives,[41,42] compositional engineering,[43,44] and solvent engineering.[37,45] Therefore, the resultant J_{sc} and PCE values of the n-BA+-based PSCs in this work are quite low, consistent with previous reports.[6,31,46,47] Fortunately, the replacement from n-BA+ to iso-BA+ gives rise to a substantially improved average PCE of ~15% with a much higher J_{sc} of ~20 mA cm−2. The J_{sc} values are verified by the external quantum efficiency (EQE) results with errors smaller than 5% in Figure 1h. The small hysteresis was possibly due to ion-migration-induced charge accumulation along the vertical direction.[48,49] Interestingly, while the carrier lifetime in the PSCs based on the two ligands was comparative with the iso-BA+-based one being 10 μs higher (Figure S10a and Table S1, Supporting Information), a huge difference in charge transfer resistance (R_{ct}) was observed by electrochemical impedance spectroscopy (EIS) measurements (Figure S10b and Table S1, Supporting Information). The R_{ct} value of the n-BA+-based device is four orders of magnitude larger than that of the iso-BA+-based device, indicating that the charge extraction is greatly obstructed in the n-BA+-based devices, which is responsible for the lower J_{sc}. Considering the similar film thicknesses (Figure S11, Supporting Information) and absorption spectra (Figure S7, Supporting Information) between n-BA+ and iso-BA+-based perovskite films, we believe that the significantly lower J_{sc} and larger R_{ct} in the n-BA+-based devices are most likely related to the observed much lower crystallinity and orientational order of the n-BA+-based perovskite film.

2.2. Crystallization Kinetics of 2D Perovskite Films Based on Isomeric Ligands

To examine the origin of the distinct film orientation and crystallinity with different isomeric ligands, synchrotron-based in situ GIWAXS techniques were utilized to monitor perovskite crystallization pathways during the film fabrication process.[50] To achieve full penetration of X-ray in the films, an incident angle of 2° was used for the in situ GIWAXS measurements, confirmed by the signal of ITO substrate (see Experimental Section for details). The crystallization process of the n-BA+-based perovskite film was first investigated and four crystallization stages were identified. The representative 2D GIWAXS patterns for each stage are displayed in **Figure 2**a, together with the corresponding intensity profiles along the q_z direction (Figure 2c), versus q_r at a constant $q_z = 1.00$ Å−1 (Figure 2d), and along the polar angle χ at $q = 1.00$ Å−1 (Figure 2e) (see Figure S12 and Note S2, Supporting Information, for details about the different integration directions). It was found that at the initial stage (Stage I), there is a signal of colloidal sol–gels at $q \approx 0.5$ Å−1,[35] and three peaks located at $q \approx 1.5$, 2.1, and 2.5 Å−1 which are from the ITO substrate. As the spinning continues, the intensity of the sol–gels decreases while multifarious peaks arise at stage II. These peaks are attributed to vertical 3D and multi-oriented perovskite phases (Figure 2c–e Stage II). Next, the appearance of the (1 2n+1 1) peak at $q_r = 0.89$ Å−1 and $q_z = 1.00$ Å−1 from 2D perovskites indicates that the crystallization process enters Stage III. In the meantime, the precursor residue persists in the film at this stage, coexisting with the crystalline

phases. These 3D/2D perovskite phases remain at Stage IV after the precursor is consumed entirely (Figure 2c–e Stage IV). In contrast, the iso-BA+-based perovskite demonstrates a simpler crystallization pathway that involves only three stages: 1) precursor stage; 2) precursor + vertical 2D/3D; 3) vertical 2D/3D, as shown in Figure 2b. The multi-oriented perovskite phases were not observed throughout the processes (Figure 2f–h). Instead, the 2D perovskite phase emerges as early as stage II, as indicated by the appearance of (1 2n+1 1) peak in Figure 2g.

To further understand the crystallization process kinetically, we summarize the in situ GIWAXS intensity profiles of the perovskites based on n-BA+ and iso-BA+ in the form of false-color intensity maps versus q_z, q_r at $q_z = 1.00$ Å−1, or polar angle χ (y-axis) and spinning time (x-axis) in **Figure 3** and Figure S13, Supporting Information. Here, we use (220) peak at (q_r, q_z) = (1.41, 1.00) Å−1 to represent corner-stacked [PbI$_6$] frameworks from vertical 3D phases, the (1 2n+1 1) peak along the q_r direction at $q_z = 1.00$ Å−1 to represent the vertical 2D phase, and the peak at polar angle $\chi = 47°$ at $|q| = 1.00$ Å−1 to represent multi-oriented phases, respectively. At the beginning of the spin coating process, both perovskites with n-BA+ and iso-BA+ ligands experience a similar stage I, which mainly consists of the scattering signal of sol–gel solution colloids centered at $q \approx 0.5$ Å−1 and lasts for 5 s due to the gradual removal of N, N-dimethylformamide (DMF) molecules[51,52] (Figure 3a,d). Subsequently, the isomeric ligands with linear and branched structures give rise to divergent perovskite crystallization routes. For the n-BA+-based perovskites, the vertical and multi-oriented perovskite phases emerge simultaneously at the 5th second of spinning (Figure 3a and Figures S13a and S14a, Supporting Information), indicating the onset of stage II. These phases quickly build up by consuming the precursors during stage II, as revealed by the corresponding evolutions of the peak areas in Figure 3c. The system enters stage III at the 8th second when the (220) peak of the vertical 3D perovskite phases and the (1 2n+1 1) peak of the 2D perovskite phase arise at the same time (Figure 3b,c). The peak area of the vertical 2D and 3D perovskite phase is enhanced slowly and reaches a plateau in around 10 s at the expense of precursors during stage III (Figure 3c), implying a slow phase transition from the residual precursor to the vertical 3D and 2D perovskites. It is noted that the n-BA+-based perovskite precursors persist in the film for a long time and do not disappear entirely until the 18th second of spinning at the end of stage III. After the precursors disappear, the vertical 3D, multi-oriented, and 2D perovskites coexist and remain stable in the film during final stage IV, which is consistent with the ex situ GIWAXS results of the final perovskite film in Figure 1b. For the iso-BA+-based system, the precursor signal vanishes in 8 s (Figure 3d and Figures S13b and S14b, Supporting Information), and the vertical 3D and 2D perovskite phases appear simultaneously at the 5th second and rapidly accumulate to a high population in only 3 s during stage II, as shown in Figure 3e,f, and then the system enters stage III with the coexistence of the vertical 2D and vertical 3D perovskites without the multi-oriented phases. The crystallization pathways of perovskites based on n-BA+ and iso-BA+ ligands are summarized in Figure 3g. It is suggested that the branched iso-BA+ ligands not only accelerate the film crystallization process but also promote the formation of vertical 2D perovskites.
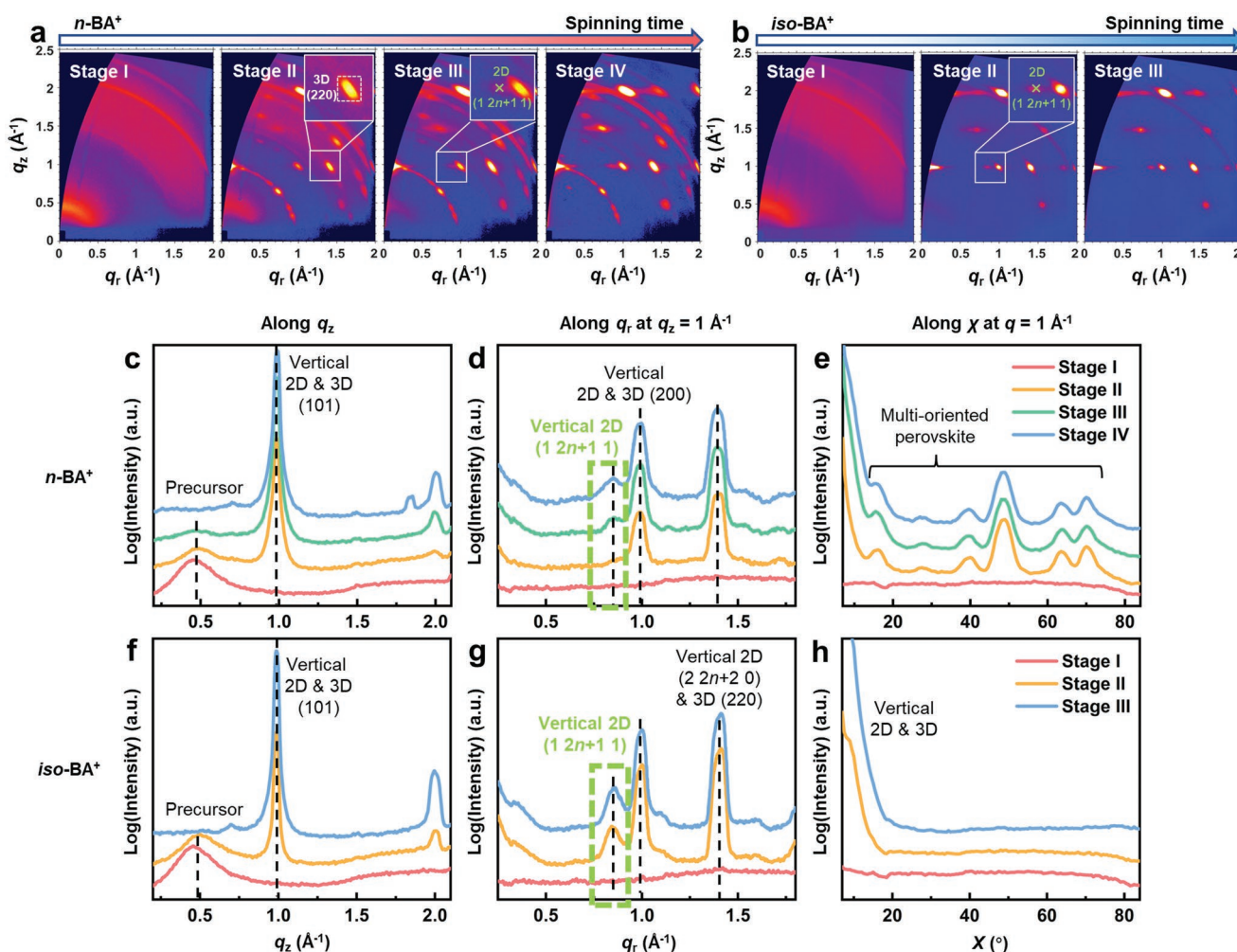
Figure 2. Crystallization kinetics of 2D perovskite films based on isomeric ligands. a,b) Representative GIWAXS patterns at different crystallization stages during the spin coating process of the perovskite films based on a) n-BA$^+$ and b) iso-BA$^+$ ligands, where the insets highlight the emergence of the vertical-2D (1 2n+1 1) peak. c–e) The GIWAXS intensity profiles for the n-BA$^+$-based perovskite film c) along q_z direction, d) along q_r direction at $q_z = 1.00$ Å^{-1}, and e) along polar angle χ at $q = 1.00$ Å^{-1}. f–h) The GIWAXS intensity profiles for the iso-BA$^+$-based perovskite film f) along q_z direction, g) along q_r direction at $q_z = 1.00$ Å^{-1}, and h) along polar angle χ at $q = 1.00$ Å^{-1}.

Moreover, the growth of the unwanted multi-oriented perovskites is completely suppressed with the presence of iso-BA$^+$ ligands since the onset of crystallization.

2.3. Formation Mechanism of Micron-Sized Clusters in iso-BA$^+$-Based Precursor Solutions

Interestingly, the precursor solutions based on n-BA$^+$ and iso-BA$^+$ ($<n> = 5$) are notably different. The iso-BA$^+$-based perovskite precursor is counterintuitively turbid, implying the presence of large clusters, while the precursor with n-BA$^+$ ligands is clear, as shown in the inset of **Figure 4**a. DLS measurements were carried out to estimate the averaged aggregation size in the two perovskite precursor solutions. It was found that the size in the clear n-BA$^+$-based solution is only several nanometers whereas the iso-BA$^+$-based one has "clusters" with the size of several microns. The composition of these sediments

was unknown since they could be the aggregation of pure iso-BA$^+$ ligands, some reaction products, or a mixture of raw materials. A series of experiments and characterizations were conducted as follows to figure it out. The same concentration of iso-butylammonium iodide (iso-BAI) was fully dissolved in DMF (0.4 M) (Figure S15, Supporting Information), proving that the turbidity was not due to the low solubility of iso-BAI. Also, the clusters still existed after the iso-BA$^+$-based perovskite solution was diluted to 0.8 and 0.6 M and well mixed by a high-speed vortex mixer (Figure S16, Supporting Information). The GIWAXS patterns of the perovskite film fabricated by the diluted solutions showed completely the same as the original one (Figure S17, Supporting Information). Although these large clusters can be removed by filtering, the resulting devices fabricated from the filtered iso-BA$^+$-based precursor showed inferior performance (Figure S18, Supporting Information), indicating that these clusters must contribute to the formation of perovskites. To reveal the composition of the clusters, we separated
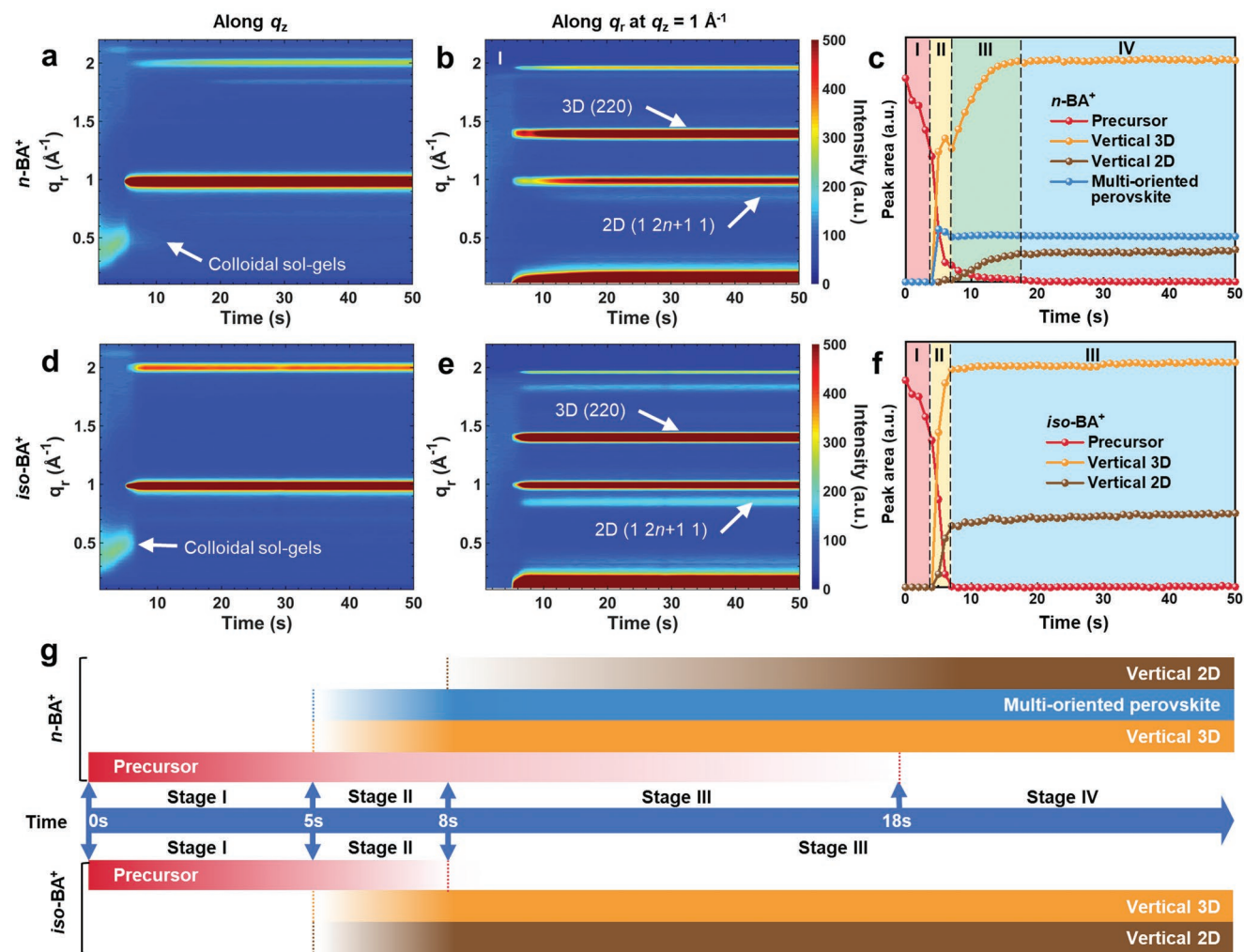
Figure 3. Perovskite film formation analysis during spin coating. a,d) The false-color GIWAXS intensity maps versus q_z and spinning time based on a) n-BA$^+$ and d) iso-BA$^+$. b,e) The false-color GIWAXS intensity maps versus q_r at $q_z = 1.00$ Å^{-1} and spinning time based on b) n-BA$^+$ and e) iso-BA$^+$. c,f) The corresponding time evolutions of peak areas of each phase based on c) n-BA$^+$ and f) iso-BA$^+$. g) The phase evolution schematic diagram in the first 25 s of the spin coating process for both perovskite systems.

them from solutions by centrifugation and conducted hydrogen nuclear magnetic resonance (^{1}H-NMR) measurements, as shown in Figure 4b and Figure S19, Supporting Information. Here, we consider the centrifugation did not cause a change in the clusters by showing that the cluster size remained unchanged after shaking up the vessel to uniformly re-disperse the clusters after centrifugation (Figure S20, Supporting Information). The NMR results suggest the existence of MA$^+$ and iso-BA$^+$ in the cluster, with a molar ratio of 1.95:1, which is very close to the stoichiometric ratio of 2:1 in the $<n>$ = 5 perovskite precursor. Furthermore, I:Pb ratios from 20 random positions of the clusters were also examined by energy-dispersive X-ray spectroscopy (EDX) (Figure 4c). The I:Pb ratios are normally distributed with a mean value of 3.16, which also agree well with the stoichiometric ratio of 3.2 in $<n>$ = 5 RP perovskites (red dashed line in Figure 4c). In light of both NMR and EDX results, the clusters are found to share almost the same composition with the $<n>$ = 5 iso-BA$^+$-based perovskite precursor, implying that these clusters could serve as pre-nucleation

centers for the crystallization of 2D perovskites. Consequently, the formation of 2D perovskites is accelerated and precursors are consumed more quickly, as observed by in situ GIWAXS (Figure 3). It is worth mentioning that pre-nucleation clusters were observed in all iso-BA$^+$-based perovskite precursor solutions regardless of the $<n>$ values, as shown in the right four photos of Figure 4d and Figure S21, Supporting Information. In comparison, the n-BA$^+$-based solutions are all clear, as shown in the left four photos of Figure 4d. Thus, it suggests that the formation of the clusters is mainly determined by the ligand structure.

To understand the formation mechanism of the pre-nucleation cluster, we calculate the formation energies of molecular clusters based on n-BA$^+$ or iso-BA$^+$ using DFT calculations. For each of the isomeric BA$^+$ cations, two interaction geometries are defined, called head-head (NH$_3^+$-NH$_3^+$) and tail-tail (C$_x$H$_y$-C$_x$H$_y$), which mimic the geometry of nearest neighbor ligands in the 2D perovskite crystals in the [020] direction and the [101] direction, respectively (Figure 4e,f).
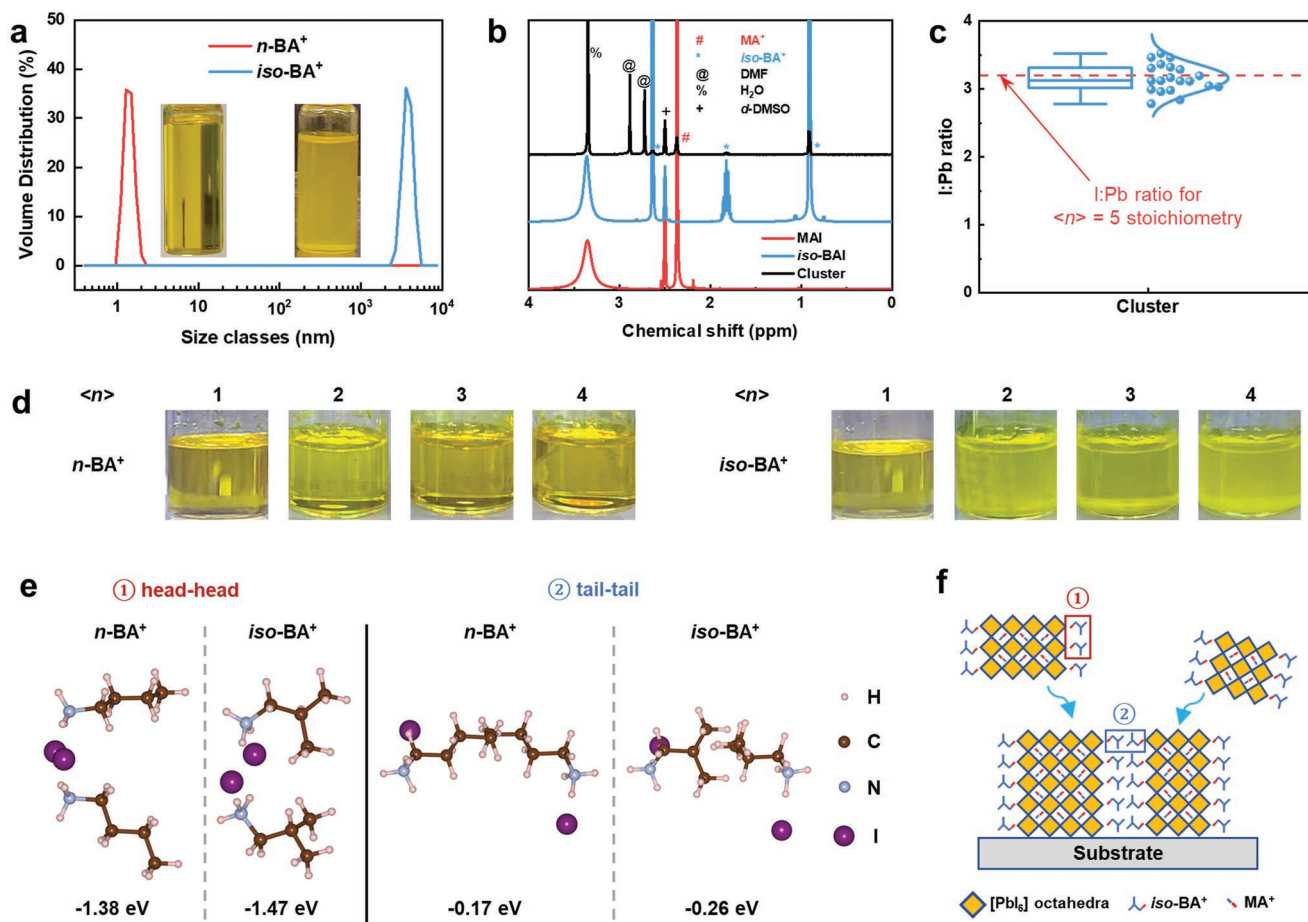
Figure 4. Formation mechanism of micron-sized clusters in iso-BA+-based precursor solutions. a) Dynamic light scattering (DLS) results and photos of the $\langle n \rangle$ = 5 perovskite precursors with n-BA$^+$ (left) and iso-BA$^+$ (right). b) ^{1}H-NMR results of pure MAI, pure iso-BA$^+$, and the clusters from the iso-BA$^+$-based perovskite precursor dissolved in deuterated-DMSO. c) Statistical atomic I/Pb ratios (20 positions) of the clusters measured by EDX. d) Photos of $\langle n \rangle$ = 1 to 4 perovskite precursor solutions with n-BA$^+$ (left) and iso-BA$^+$ (right), where the solution of iso-BA$^+$ $\langle n \rangle$ = 1 is confirmed by DLS (see Figure S12, Supporting Information). e) Optimized structures of n-BA$^+$ and iso-BA$^+$-based molecular clusters in the interaction modes of head-head (NH$_3^+$-NH$_3^+$) and tail-tail (C$_x$H$_y$-C$_x$H$_y$). The numbers are formation energies (in eV) of the molecular clusters. f) Scheme of the crystallization mechanism of the iso-BA$^+$-based 2D perovskite.

Detailed structures are given in Figure S22, Supporting Information. Our results indicate that regardless of the interaction geometry, the aggregation of the iso-BA$^+$ molecular cluster is always more favorable than that of n-BA$^+$, as binding between every two iso-BAI molecules is stronger by ~0.1 eV. This results from iso-BA$^+$ clusters being spatially more compact than n-BA$^+$ clusters (Figure 4e), as iso-butyl side chains are more compact than the linear n-butyl side chains. A more compact cluster gives a stronger electrostatic and van der Waals bonding (see Figure S23 and Note S4, Supporting Information). As shown in the scheme of Figure 4f, we propose that the crystallization of the iso-BA$^+$-based 2D perovskite is promoted in two ways. First, the strong head-head interaction makes the pre-nucleation of 2D perovskite fragments more favorable. Second, these perovskite fragments are merged via tail-tail interactions. This analysis is consistent with our experimental findings in the iso-BA$^+$-based systems, where the formation of micron-sized clusters is found in the precursor solutions (Figure 4a,d).

2.4. Formation Mechanism of Multi-Oriented Phases and the n-Value Dependence

Another major difference between the iso-BA$^+$ and the n-BA$^+$-based systems is the occurrence of a multi-oriented perovskite phase in the latter case (Figures 1b and 2e). This is possibly a result of the substitution of MA$^+$ by n-BA$^+$ in the 3D perovskite. To confirm this hypothesis, we calculate the reaction enthalpy of the following reaction

$$MAPbI_3 + BAI \rightarrow (BA, MA)PbI_3 + MAI \quad (1)$$
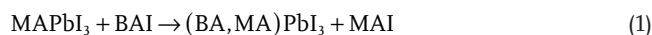
where BA represents n-BA$^+$ or iso-BA$^+$. Details of the structural models and computational settings are described in the Experimental Section – Computational Methods. Our calculations show that the substitution of a small amount of MA$^+$ (~3%) by n-BA$^+$ is favorable, with a negative reaction enthalpy of −0.12 eV per substituted molecule. The linear n-BA$^+$ molecule can easily straddle between two cubes so that it can be better accommodated by the

perovskite lattice, as compared to the more spherical *iso*-BA⁺ molecule, as shown in **Figure 5**a. Despite the favorable incorporation of *n*-BA⁺ at a low percentage, because of its large size, its incorporation becomes unfavorable with increasing substitution of MA⁺ by *n*-BA⁺. In other words, the *n*-BA⁺ ion is too large to occupy

the A site while keeping a perovskite structure. According to the empirical Goldschmidt tolerance factor[53]

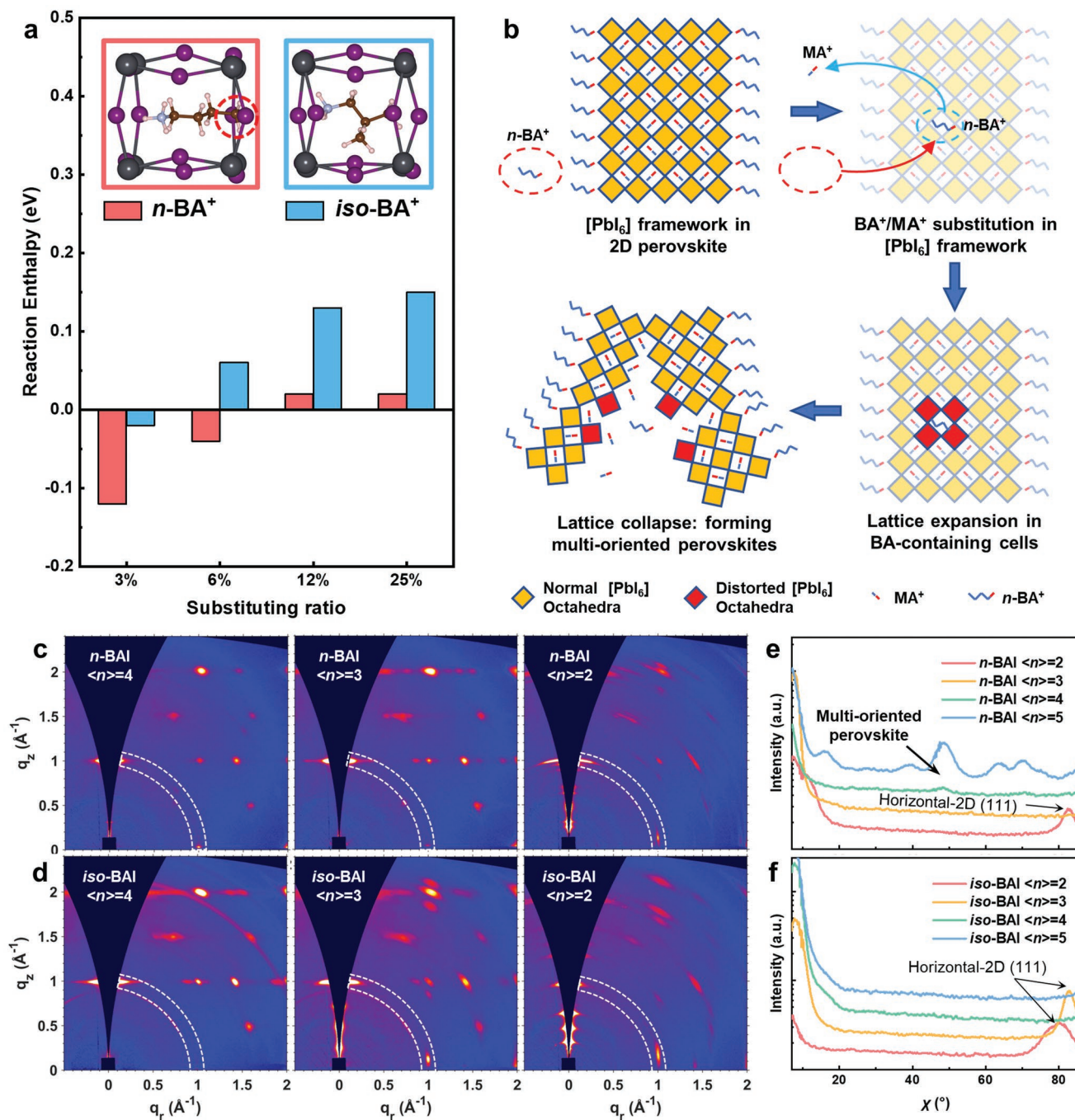$$t = \frac{r_A + r_X}{\sqrt{2}(r_B + r_X)} \qquad (2)$$

Figure 5. Formation mechanism of multi-oriented phases and the *n*-value dependence. a) Reaction enthalpies of substituting MA⁺ with *n*-BA⁺ or *iso*-BA⁺ in MAPbI₃, and optimized configurations of *n*-BA⁺ and *iso*-BA⁺ in a MAPbI₃ lattice, where only one Pb-I cube is shown. The dashed circle highlights the stretch of *n*-BA⁺ out of the cube. b) Schematic of the formation process of multi-oriented perovskite phases. c,d) The ex situ GIWAXS patterns of the 2D perovskite films based on c) *n*-BA⁺ and d) *iso*-BA⁺ with different ⟨*n*⟩ values. e,f) The corresponding intensity profiles based on e) *n*-BA⁺ and f) *iso*-BA⁺ along polar angle χ at $q = 1$ Å⁻¹.

The substitution of MA^+ by BA^+ will engender an increased t of 1.7, which is far beyond the acceptable range of 0.8–1 for a stable perovskite lattice. Therefore, the highly unstable BA-substituted $MAPbI_3$ phase is prone to distort and collapse immediately once BA^+ replaces MA^+ considering that expanded lattice cannot maintain the distance among ions for Pb—I—Pb bonding. Meanwhile, other MA-containing unit cells that connect with the collapsed ones keep the perovskite structure, but the orientation is affected away from the vertical/horizontal orientational alignment and hence the $[PbI_6]$ framework becomes fragmented,[54] forming the multi-oriented perovskites, as illustrated in Figure 5b. The calculation conducted in the $MAPbI_3$ lattice is to demonstrate the process in the $[PbI_6]$ octahedral framework. In fact, the multi-oriented perovskites can be generated from both 2D and 3D phases, because their formation is due to the substitution of MA^+ by n-BA^+ which can occur in the $[PbI_6]$ octahedral framework in both 2D and 3D perovskites. This result explains the origin of the multi-oriented phases in the GIWAXS patterns of the $<n> = 5$ n-BA^+ based perovskite. In contrast, the substitution of MA^+ by iso-BA^+ only gives a negative reaction enthalpy at 3% substitution with quite a small magnitude (−0.02 eV) very close to zero, showing that the substitution of MA^+ by iso-BA^+ is very unlikely to happen. Therefore, in the iso-BA^+-based perovskites, the amount of iso-BA-substituted unit cells would be too small to be observed, if there were any of them.

The growth of the multi-oriented perovskite phases in the n-BA^+-based film is also found to be related to the $<n>$ value, namely the ratio of MA^+ to BA^+. As shown in Figure 5c,e, the $<n> = 4$ perovskite film based on n-BA^+ ligand also exhibits a multi-oriented phase similar to that in the $<n> = 5$ perovskite film (see Figure S24, Supporting Information, for peak labeling), albeit with a weaker intensity. As the value of $<n>$ decreases, the peaks from the vertical 3D phase become weaker and concurrently the signals from the multi-oriented perovskite phases disappear completely. Instead, highly ordered 2D perovskite phases are formed (e.g., $<n> = 2$). This is consistent with the phenomenon reported in a previous work that a lower $<n>$ system would have fewer 3D phases because of the log-normal distribution of n number centered near the expected average $<n>$ set by the precursor ratios.[37] In other words, the formation of the multi-oriented phase can be also suppressed by a lower $<n>$ value. However, a 2D perovskite system with a lower $<n>$ value tends to grow 2D perovskite horizontally, which is detrimental to device performance.[15,19] The formation of horizontally oriented 2D perovskite phase is observed in the n-BA^+-based film when $<n> = 2$. The peak at around $\chi = 80°$ corresponds to the (111) plane from horizontal 2D phases (Figure 5e). Similarly, the horizontal-2D phase is also found in iso-BA^+-based films when $<n> = 3$ and 2 (Figure 5d,f, see Figures S25 and S26, Supporting Information, for peak labeling). However, none of the iso-BA^+-based films with different $<n>$ values present multi-oriented perovskite peaks in the GIWAXS patterns.

3. Conclusion

In summary, we have systematically investigated the influence of isomeric ligand structure on the crystallization kinetics and film properties of 2D perovskite films. A simple alteration from linear n-BA^+ to branched iso-BA^+ molecule surprisingly leads to a rather superior device performance due to better crystal orientation and improved film crystallinity. From in situ GIWAXS results, we conclude that the formation of vertical and multi-oriented perovskite phases in the n-BA^+-based system is easier than that of the 2D perovskite. In contrast, the branched iso-BA^+ ligands are able to not only promote the crystallization of 2D perovskites but also inhibit the formation of unwanted multi-oriented perovskites. DFT calculations suggest that the superior performance of iso-BA^+ can be ascribed to two factors. First, the formation of iso-BA^+ molecular clusters in the precursor solution is favored, which may provide nucleation centers for the growth of vertical 2D perovskites. Second, an iso-BA^+ cation cannot be incorporated in a 3D perovskite lattice, which obstructs the formation of multi-oriented phases, promoting a long-range vertically oriented $[PbI_6]$ framework stacking. This work provides an in-depth understanding of how a simple structural difference of the A′-site ligand influences the crystallization and orientation of both 2D and 3D phases in 2D perovskite systems, and paves the way toward further development of high-performance 2D perovskite optoelectronic devices.

4. Experimental Section

Materials: DMF (99.8%, anhydrous), dimethyl sulfoxide (DMSO, 99.8%, anhydrous), silver (99.9%), and bathocuproine (BCP, 96%) were purchased from Sigma-Aldrich. Methylammonium iodide (MAI) was purchased from Dyesol. N-butylammonium iodide (n-BAI), iso-BAI, lead iodide (II) (PbI_2), and (6,6)-phenyl-C_{61}-butyric acid methyl ester ($PC_{61}BM$) were purchased from Xi'an Polymer Light Technology Corp. Poly(3,4-ethylenedioxythiophene) polystyrene sulfonate (PEDOT:PSS, Al 4083) was purchased from Ossila. All the chemicals were used as received without further purification.

Precursor Solution Preparation: $BA_2MA_4Pb_5I_{16}$ ($<n> = 5$) perovskite precursor solutions were prepared by mixing n-BAI (or iso-BAI), MAI, and PbI_2 in a stoichiometric ratio of 2:4:5 in a DMF solution in which the concentration of Pb^{2+} was 1 mmol mL^{-1}. The solution vessels were put on a vortex mixer at high speed at room temperature, and the solutions were well-mixed for 1 min, respectively. Solutions of other $<n>$ values were prepared in the same methods as $<n> = 5$ ones, except changing the molar ratio of BAI, MAI, and PbI_2 into 2:0:1 for $<n> = 1$, 2:1:2 for $<n> = 2$, 2:2:3 for $<n> = 3$, and 2:3:4 for $<n> = 4$. $PCBM_{61}$ was dissolved in chloroform at a concentration of 10 mg mL^{-1}, and BCP was dissolved in isopropanol (IPA) at a concentration of 0.5 mg mL^{-1}.

Perovskite Film Fabrication: ITO glasses were successively cleaned in the detergent aqueous solution once, in deionized water twice, in acetone once, and in IPA once in hypersonic cleaner. The clean ITO glasses were then blown dry and treated with UV-ozone for 30 min. The PEDOT:PSS solution was spin-coated onto the ITO substrates at 4000 rpm for 30 s, and then annealed at 130 °C for 30 min in air ambient. The coated substrates were transferred into a nitrogen-filled glovebox. The substrates were heated to 100 °C before use, and the perovskite precursor solution was heated to 80 °C. The perovskite films were spin-coated onto the substrates at 5000 rpm for 20 s and were immediately annealed at 100 °C for 10 min, for all the fabrication conditions.

Device Fabrication: Followed by perovskite film fabrication, PCBM (10 mg mL^{-1} in chloroform) and BCP (0.5 mg mL^{-1} in IPA) solutions were subsequently spin-coated both at 4000 rpm for 20 s. Finally, 100 nm silver electrode was thermal evaporated onto the films through rectangle-shaped masks.

**ADVANCED
SCIENCE NEWS**

www.advancedsciencenews.com

NANO · MICRO

small

www.small-journal.com

Characterization: The current density–voltage (*J*–*V*) curves were measured by Keithley 2400 source meter under an AM 1.5G simulating source from Enlitech Solar Simulator, which was calibrated by the reference cell before measurements. The specific parameters of the *J*–*V* scan are as follows: the interval was 50 ms; the step was 0.01 V; the range was from −0.2 to 1.4 V; no device preconditioning prior to testing was conducted; the testing condition was in an N_2-filled glovebox at room temperature (~25 °C); no antireflection coating was used; the device contact area was 4.50 mm^2 defined by mask and was calibrated by an optical microscope; the whole devices were illuminated; the reference cell was calibrated in May 2017. EQE results were measured by the Enlitech Photovoltaic Quantum Efficiency system. UV–vis absorption measurements were carried out by using PerkinElmer LAMBDA 950 UV/vis/NIR Spectrophotometer. EIS measurements were conducted using the Zahner Electrochemical workstation. Scanning electron microscopy (SEM) images and energy dispersive X-ray spectroscopy were obtained by JEOL JSM-7800F Schottky Field Emission Scanning Electron Microscope. Transmission electron microscopy (TEM) images were obtained by FEI TS12. Ex situ and in situ GIWAXS data were collected at 23A small- and wide-angle X-ray scattering (SWAXS) beamline in the National Synchrotron Radiation Research Center (NSRRC), Hsinchu, Taiwan, R.O.C. The wavelength was 1.240 Å (10 keV), and the incident angle was 0.3° for ex situ measurement and 2° for in situ measurement to eliminate twin peaks originated by multiple reflections in the films. To conduct the hot-casting process, ITO substrates were fixed on an iron block that possesses a high heat capacity and they were heated together before the experiment. The substrate temperature can be almost maintained at 100 °C for 50 s during the in situ spin coating process. Background subtraction was conducted for all the GIWAXS data of the samples right after the raw data were acquired to reduce strong diffuse scattering near the direct beam, by subtracting the whole GIWAXS image of a clean silicon wafer with the same parameters of the measurement. This process was finished before processing all the GIWAXS patterns and the corresponding profiles. DLS measurements were conducted by Malvern Zetasizer Nano at the required temperatures using corresponding data of DMF. ^{1}H-NMR spectra were recorded on Brucker AVANCE III 400 NMR spectrometer. Chemical shift values (δ) are expressed in parts per million using residual solvent protons as an internal standard.

Computational Methods: DFT calculations were performed with the Vienna ab initio simulation package (VASP).[55–57] The PBE-D3(BJ) functional, combining the Perdew–Burke–Ernzerhof (PBE)[58] exchange-correlation functional and the D3(BJ) scheme[59] for van der Waals interactions, was used for all calculations. A plane wave kinetic energy cutoff of 500 eV was used for calculations. The energy and force convergence criteria were set to 10^{-4} eV and 0.02 eV $Å^{-1}$, respectively. The details of DFT calculations are provided in Supporting Information.

Supporting Information

Supporting Information is available from the Wiley Online Library or from the author.

Acknowledgements

Conflict of Interest

The authors declare no conflict of interest.

Data Availability Statement

The data that support the findings of this study are available in the supplementary material of this article.

[1] H. Tsai, W. Nie, J.-C. Blancon, C. C. Stoumpos, R. Asadpour, B. Harutyunyan, A. J. Neukirch, R. Verduzco, J. J. Crochet, S. Tretiak, L. Pedesseau, J. Even, M. A. Alam, G. Gupta, J. Lou, P. M. Ajayan, M. J. Bedzyk, M. G. Kanatzidis, A. D. Mohite, *Nature* **2016**, *536*, 312.

[2] L. Mao, W. Ke, L. Pedesseau, Y. Wu, C. Katan, J. Even, M. R. Wasielewski, C. C. Stoumpos, M. G. Kanatzidis, *J. Am. Chem. Soc.* **2018**, *140*, 3775.

[3] T. Luo, Y. Zhang, Z. Xu, T. Niu, J. Wen, J. Lu, S. Jin, S. Liu, K. Zhao, *Adv. Mater.* **2019**, *31*, 1903848.

[4] C. C. Stoumpos, D. H. Cao, D. J. Clark, J. Young, J. M. Rondinelli, J. I. Jang, J. T. Hupp, M. G. Kanatzidis, *Chem. Mater.* **2016**, *28*, 2852.

[5] Z. Wang, Q. Lin, F. P. Chmiel, N. Sakai, L. M. Herz, H. J. Snaith, *Nat. Energy* **2017**, *2*, 17135.

[6] X. Zhang, G. Wu, S. Yang, W. Fu, Z. Zhang, C. Chen, W. Liu, J. Yan, W. Yang, H. Chen, *Small* **2017**, *13*, 1700611.

[7] K. Zheng, Y. Chen, Y. Sun, J. Chen, P. Chábera, R. Schaller, M. J. Al-Marri, S. E. Canton, Z. Liang, T. Pullerits, *J. Mater. Chem.* **2018**, *6*, 6244.

[8] N. Zhou, B. Huang, M. Sun, Y. Zhang, L. Li, Y. Lun, X. Wang, J. Hong, Q. Chen, H. Zhou, *Adv. Energy Mater.* **2020**, *10*, 1901566.

[9] C. J. Dahlman, R. A. DeCrescent, N. R. Venkatesan, R. M. Kennard, G. Wu, M. A. Everest, J. A. Schuller, M. L. Chabinyc, *Chem. Mater.* **2019**, *31*, 5832.

[10] C. Liang, H. Gu, Y. Xia, Z. Wang, X. Liu, J. Xia, S. Zuo, Y. Hu, X. Gao, W. Hui, L. Chao, T. Niu, M. Fang, H. Lu, H. Dong, H. Yu, S. Chen, X. Ran, L. Song, B. Li, J. Zhang, Y. Peng, G. Shao, J. Wang, Y. Chen, G. Xing, W. Huang, *Nat. Energy* **2021**, *6*, 38.

[11] X. Zhang, G. Wu, W. Fu, M. Qin, W. Yang, J. Yan, Z. Zhang, X. Lu, H. Chen, *Adv. Energy Mater.* **2018**, *8*, 1702498.

[12] W. Fu, J. Wang, L. Zuo, K. Gao, F. Liu, D. S. Ginger, A. K. Y. Jen, *ACS Energy Lett.* **2018**, *3*, 2086.

[13] J. Zhang, J. Qin, M. Wang, Y. Bai, H. Zou, J. K. Keum, R. Tao, H. Xu, H. Yu, S. Haacke, B. Hu, *Joule* **2019**, *3*, 3061.

[14] Y. Yang, C. Liu, A. Mahata, M. Li, C. Roldán-Carmona, Y. Ding, Z. Arain, W. Xu, Y. Yang, P. A. Schouwink, A. Züttel, F. De Angelis, S. Dai, M. K. Nazeeruddin, *Energy Environ. Sci.* **2020**, *13*, 3093.

[15] D. H. Cao, C. C. Stoumpos, O. K. Farha, J. T. Hupp, M. G. Kanatzidis, *J. Am. Chem. Soc.* **2015**, *137*, 7843.

[16] I. C. Smith, E. T. Hoke, D. Solis-Ibarra, M. D. McGehee, H. I. Karunadasa, *Angew. Chem., Int. Ed.* **2014**, *53*, 11232.

[17] H. Zheng, G. Liu, L. Zhu, J. Ye, X. Zhang, A. Alsaedi, T. Hayat, X. Pan, S. Dai, *Adv. Energy Mater.* **2018**, *8*, 1800051.

**ADVANCED
SCIENCE NEWS**

www.advancedsciencenews.com

NANO · MICRO

small

www.small-journal.com

[18] C. Ge, J.-F. Lu, M. Singh, A. Ng, W. Yu, H. Lin, S. Satapathi, H. Hu, *Sol. RRL* **2022**, *6*, 2100879.

[19] A. Z. Chen, M. Shiu, J. H. Ma, M. R. Alpert, D. Zhang, B. J. Foley, D.-M. Smilgies, S.-H. Lee, J. J. Choi, *Nat. Commun.* **2018**, *9*, 1336.

[20] D. Liang, C. Dong, L. Cai, Z. Su, J. Zang, C. Wang, X. Wang, Y. Zou, Y. Li, L. Chen, L. Zhang, Z. Hong, A. El-Shaer, Z.-K. Wang, X. Gao, B. Sun, *Small* **2021**, *17*, 2100972.

[21] L. Yan, J. Hu, Z. Guo, H. Chen, M. F. Toney, A. M. Moran, W. You, *ACS Appl. Mater. Interfaces* **2018**, *10*, 33187.

[22] X. Lian, H. Wu, L. Zuo, G. Zhou, X. Wen, Y. Zhang, G. Wu, Z. Xie, H. Zhu, H. Chen, *Adv. Funct. Mater.* **2020**, *30*, 2004188.

[23] J. Hu, I. W. H. Oswald, S. J. Stuard, M. M. Nahid, N. Zhou, O. F. Williams, Z. Guo, L. Yan, H. Hu, Z. Chen, X. Xiao, Y. Lin, Z. Yang, J. Huang, A. M. Moran, H. Ade, J. R. Neilson, W. You, *Nat. Commun.* **2019**, *10*, 1276.

[24] W. Fu, H. Liu, X. Shi, L. Zuo, X. Li, A. K. Y. Jen, *Adv. Funct. Mater.* **2019**, *29*, 1900221.

[25] H. Lai, D. Lu, Z. Xu, N. Zheng, Z. Xie, Y. Liu, *Adv. Mater.* **2020**, *32*, 2001470.

[26] J. Liang, Z. Zhang, Q. Xue, Y. Zheng, X. Wu, Y. Huang, X. Wang, C. Qin, Z. Chen, C.-C. Chen, *Energy Environ. Sci.* **2022**, *15*, 296.

[27] M. Shao, T. Bie, L. Yang, Y. Gao, X. Jin, F. He, N. Zheng, Y. Yu, X. Zhang, *Adv. Mater.* **2022**, *34*, 2107211.

[28] J. Shi, Y. Gao, X. Gao, Y. Zhang, J. Zhang, X. Jing, M. Shao, *Adv. Mater.* **2019**, *31*, 1901673.

[29] Z. Yao, Y. Zhou, X. Yin, X. Li, J. Han, M. Tai, Y. Zhou, J. Li, F. Hao, H. Lin, *CrystEngComm* **2018**, *20*, 6704.

[30] X. Li, J. Hoffman, W. Ke, M. Chen, H. Tsai, W. Nie, A. D. Mohite, M. Kepenekian, C. Katan, J. Even, M. R. Wasielewski, C. C. Stoumpos, M. G. Kanatzidis, *J. Am. Chem. Soc.* **2018**, *140*, 12226.

[31] Y. Chen, Y. Sun, J. Peng, W. Zhang, X. Su, K. Zheng, T. Pullerits, Z. Liang, *Adv. Energy Mater.* **2017**, *7*, 1700162.

[32] X. Li, J. M. Hoffman, M. G. Kanatzidis, *Chem. Rev.* **2021**, *121*, 2230.

[33] X. Meng, Y. Li, Y. Qu, H. Chen, N. Jiang, M. Li, D.-J. Xue, J.-S. Hu, H. Huang, S. Yang, *Angew. Chem., Int. Ed.* **2021**, *60*, 3693.

[34] H. Hu, M. Qin, P. W. K. Fong, Z. Ren, X. Wan, M. Singh, C.-J. Su, U.-S. Jeng, L. Li, J. Zhu, M. Yuan, X. Lu, C.-W. Chu, G. Li, *Adv. Mater.* **2021**, *33*, 2006238.

[35] J. M. Hoffman, J. Strzalka, N. C. Flanders, I. Hadar, S. A. Cuthriell, Q. Zhang, R. D. Schaller, W. R. Dichtel, L. X. Chen, M. G. Kanatzidis, *Adv. Mater.* **2020**, *32*, 2002812.

[36] X. Zhang, R. Munir, Z. Xu, Y. Liu, H. Tsai, W. Nie, J. Li, T. Niu, D.-M. Smilgies, M. G. Kanatzidis, A. D. Mohite, K. Zhao, A. Amassian, S. Liu, *Adv. Mater.* **2018**, *30*, 1707166.

[37] R. Quintero-Bermudez, A. Gold-Parker, A. H. Proppe, R. Munir, Z. Yang, S. O. Kelley, A. Amassian, M. F. Toney, E. H. Sargent, *Nat. Mater.* **2018**, *17*, 900.

[38] X. Zhang, X. Ren, B. Liu, R. Munir, X. Zhu, D. Yang, J. Li, Y. Liu, D.-M. Smilgies, R. Li, Z. Yang, T. Niu, X. Wang, A. Amassian, K. Zhao, S. Liu, *Energy Environ. Sci.* **2017**, *10*, 2095.

[39] L. Kuai, J. Li, Y. Li, Y. Wang, P. Li, Y. Qin, T. Song, Y. Yang, Z. Chen, X. Gao, B. Sun, *ACS Energy Lett.* **2020**, *5*, 8.

[40] P. Scherrer, in *Kolloidchemie Ein Lehrbuch*, Springer, New York **1912**, pp. 387–409.

[41] K. Odysseas Kosmatos, L. Theofylaktos, E. Giannakaki, D. Deligiannis, M. Konstantakou, T. Stergiopoulos, *Energy Environ. Mater.* **2019**, *2*, 79.

[42] J. Wang, W. Wang, Y. Chen, L. Song, W. Huang, *Small Methods* **2021**, *5*, 2100829.

[43] M. Qin, H. Xue, H. Zhang, H. Hu, K. Liu, Y. Li, Z. Qin, J. Ma, H. Zhu, K. Yan, G. Fang, G. Li, U. S. Jeng, G. Brocks, S. Tao, X. Lu, *Adv. Mater.* **2020**, *32*, 2004630.

[44] B. Yang, J. Keum, O. S. Ovchinnikova, A. Belianinov, S. Chen, M.-H. Du, I. N. Ivanov, C. M. Rouleau, D. B. Geohegan, K. Xiao, *J. Am. Chem. Soc.* **2016**, *138*, 5028.

[45] Y. Rong, S. Venkatesan, R. Guo, Y. Wang, J. Bao, W. Li, Z. Fan, Y. Yao, *Nanoscale* **2016**, *8*, 12892.

[46] H. Zheng, D. Liu, Y. Wang, Y. Yang, H. Li, T. Zhang, H. Chen, L. Ji, Z. Chen, S. Li, *Chem. Eng. J.* **2020**, *389*, 124266.

[47] J. Qing, X.-K. Liu, M. Li, F. Liu, Z. Yuan, E. Tiukalova, Z. Yan, M. Duchamp, S. Chen, Y. Wang, S. Bai, J.-M. Liu, H. J. Snaith, C.-S. Lee, T. C. Sum, F. Gao, *Adv. Energy Mater.* **2018**, *8*, 1800185.

[48] R. Singh, M. Parashar, *Soft-Matter Thin Film Solar Cells*, AIP Publishing LLC, Melville, NY **2020**.

[49] E. Bi, Z. Song, C. Li, Z. Wu, Y. Yan, *Trends Chem.* **2021**, *3*, 575.

[50] M. Qin, P. F. Chan, X. Lu, *Adv. Mater.* **2021**, *33*, 2105290.

[51] Q. Hu, L. Zhao, J. Wu, K. Gao, D. Luo, Y. Jiang, Z. Zhang, C. Zhu, E. Schaible, A. Hexemer, C. Wang, Y. Liu, W. Zhang, M. Grätzel, F. Liu, T. P. Russell, R. Zhu, Q. Gong, *Nat. Commun.* **2017**, *8*, 15688.

[52] M. Qin, K. Tse, T.-K. Lau, Y. Li, C.-J. Su, G. Yang, J. Chen, J. Zhu, U.-S. Jeng, G. Li, H. Chen, X. Lu, *Adv. Mater.* **2019**, *31*, 1901284.

[53] V. M. Goldschmidt, *Naturwissenschaften* **1926**, *14*, 477.

[54] B. Saparov, D. B. Mitzi, *Chem. Rev.* **2016**, *116*, 4558.

[55] G. Kresse, J. Hafner, *Phys. Rev. B* **1993**, *47*, 558.

[56] G. Kresse, J. Furthmüller, *Phys. Rev. B* **1996**, *54*, 11169.

[57] G. Kresse, J. Furthmüller, *Comput. Mater. Sci.* **1996**, *6*, 15.

[58] S. Grimme, S. Ehrlich, L. Goerigk, *J. Comput. Chem.* **2011**, *32*, 1456.

[59] J. P. Perdew, K. Burke, M. Ernzerhof, *Phys. Rev. Lett.* **1996**, *77*, 3865.